



RESEARCH LETTER

10.1029/2023GL103160

Simulation of Downward Frequency Chirping in the Rising Tone Chorus Element

Key Points:

- With a gcPIC- δf simulation in the dipole field, we reproduce the upward chirping chorus element, whose subpackets are downward chirping
- Both hole and hill structures can be formed in the $\zeta - v_{||}$ phase space, no matter whether the frequency is upward or downward chirping
- The time evolution of the hole and hill structures in the phase space leads to the alternating frequency chirping

Supporting Information:

Supporting Information may be found in the online version of this article.

Correspondence to:

H. Chen and X. Wang,
huayue_chen@foxmail.com;
wangxue@auburn.edu

Citation:

Chen, H., Wang, X., Chen, L., Omura, Y., Lu, Q., Chen, R., et al. (2023). Simulation of downward frequency chirping in the rising tone chorus element. *Geophysical Research Letters*, 50, e2023GL103160. <https://doi.org/10.1029/2023GL103160>

Received 6 FEB 2023

Accepted 21 APR 2023

Huayue Chen¹ , Xueyi Wang¹ , Lunjin Chen² , Yoshiharu Omura³ , Quanming Lu⁴ , Rui Chen⁴ , Zhiyang Xia² , and Xinliang Gao⁴

¹Department of Physics, Auburn University, Auburn, AL, USA, ²William B. Hanson Center for Space Sciences, University of Texas at Dallas, Richardson, TX, USA, ³Research Institute for Sustainable Humanosphere, Kyoto University, Kyoto, Japan, ⁴School of Geophysics and Planetary Science, University of Science and Technology of China, Hefei, China

Abstract The frequency chirping of chorus waves is commonly observed in the Earth's inner magnetosphere, but its generation remains an open question. Recently, Liu et al. (2021), <https://doi.org/10.1029/2021JA029258> reported two unusual rising-tone (upward chirping) chorus elements. Although the central frequency of constituent subpackets rises, the frequency of a single subpacket is surprisingly downward chirping. With a gcPIC- δf simulation in the dipole field, we successfully reproduce this kind of substructure, which contains alternating signs of chirping. Interestingly, both hole and hill structures are formed around the theoretical resonant velocities in the electron phase space, no matter whether the chirping is upward or downward. However, during each chirping interval, only one structure (either a hole or a hill) is associated with wave excitation: the upward chirping is related to the hole, while the hill contributes to the downward chirping. Our study provides a fresh perspective on the theory of frequency chirping in chorus waves.

Plain Language Summary The frequency chirping is a typical feature of chorus waves in the Earth's inner magnetosphere, which generally contain either rising-tone (upward chirping) elements or falling-tone (downward chirping) elements. Previous theory has suggested that the chirping is due to the nonlinear wave-particle interaction, where the hole or hill structure is formed in the electron phase space. Recently, Liu et al. (2021), <https://doi.org/10.1029/2021JA029258> have observed the upward chirping elements with their subpackets of downward chirping. What electron structure is associated with these elements becomes a puzzle. With a one-dimensional (1D) general curvilinear particle-in-cell (gcPIC) δf simulation in the dipole magnetic field, we successfully reproduce this kind of chorus element, whose frequency contains alternating upward and downward chirping. Interestingly, both the hole and hill structures are formed during a chirping interval, but only one of the two structures is responsible for wave excitation and frequency chirping. The structure of hole-hill combination provides an important clue into the theory of the frequency chirping in chorus waves.

1. Introduction

Whistler mode chorus waves are electromagnetic emissions that are commonly detected in the Earth's inner magnetosphere (Burtis & Helliwell, 1969; Horne & Thorne, 1998; Santolík et al., 2005; Tsurutani & Smith, 1974), so called since their spectra resemble those of birds chirping. These waves play a significant role in regulating electron dynamics, including the acceleration of electrons to \sim MeV energies and thus the formation of the outer radiation belt (Summers et al., 1998; Thorne et al., 2013; Xiao et al., 2014), and the precipitation of \sim 10 keV electrons into the ionosphere to produce the diffuse aurora (Nishimura et al., 2013; Thorne et al., 2010). The spectrum of chorus waves typically contains a series of discrete and repetitive elements with a frequency chirping (H. Chen et al., 2022; Gao et al., 2022; Helliwell, 1967; Ke et al., 2020; Li et al., 2013; Lu et al., 2019, 2021). The repetitive elements are considered to be caused by the continuous injection of energetic electrons from the magnetotail (H. Chen et al., 2022; Gao et al., 2022; Lu et al., 2021), while the formation of frequency chirping is still an open question.

According to the direction of frequency chirping, chorus elements generally exhibit either upward chirping (rising-tone elements) or downward chirping (falling-tone elements). The elements containing both upward and downward chirpings have also been reported (H. Chen et al., 2022; Turner et al., 2017), known as hooked-tone elements. The frequency chirping is believed to be formed by the nonlinear trapping of resonant electrons in the whistler-mode waves (H. Chen et al., 2022; Omura, 2021; Omura et al., 2008; Tao et al., 2017), where

© 2023 The Authors.

This is an open access article under the terms of the [Creative Commons Attribution-NonCommercial License](https://creativecommons.org/licenses/by/4.0/), which permits use, distribution and reproduction in any medium, provided the original work is properly cited and is not used for commercial purposes.

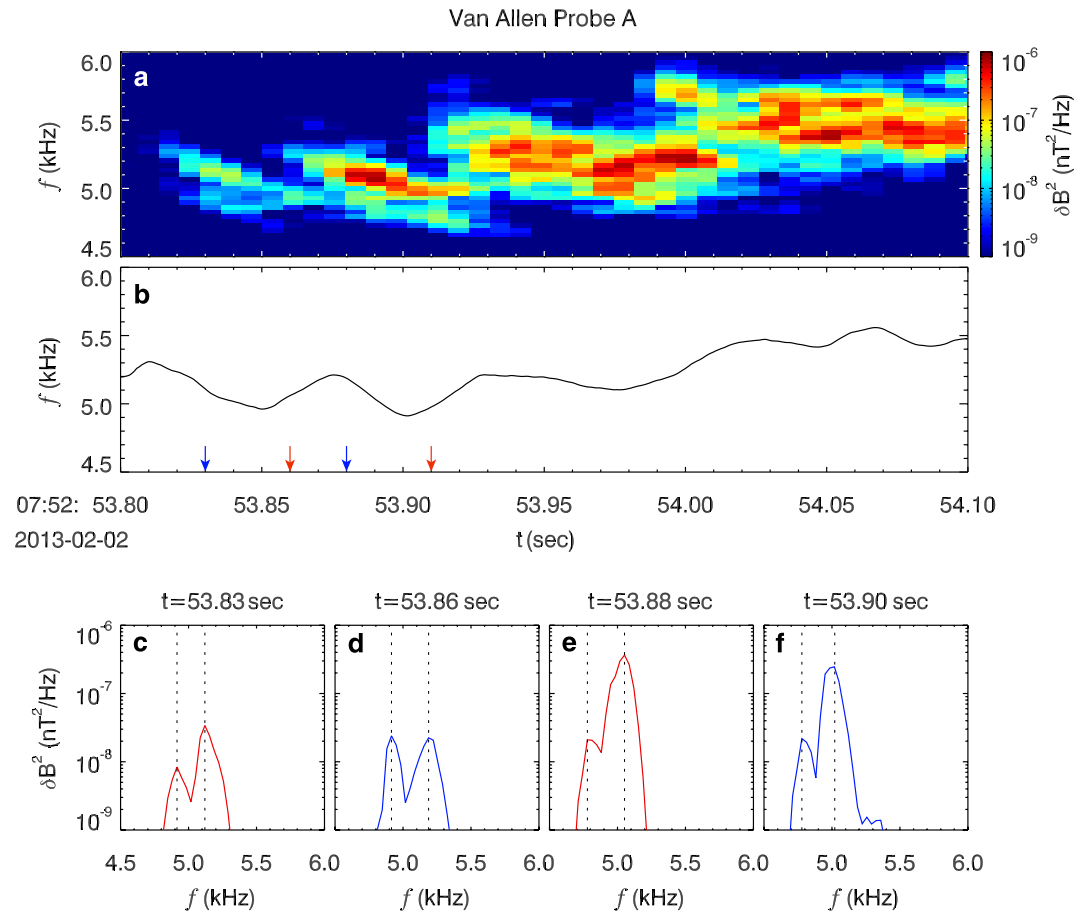


Figure 1. The example of a rising-tone chorus element with downward chirping subpackets detected by Van Allen Probe A on 2 February 2013, including the (a) spectrum of magnetic field δB^2 , (b) wave frequency f , and (c–f) δB^2 as a function of f at four selected instants denoted by the arrows. In panels (c–f), the red (blue) color represents the upward (downward) chirping intervals, and the dashed lines denote the frequencies of the two peaks (with $f = 4.81$ and 5.12 kHz, 4.91 and 5.19 kHz, 4.77 and 5.05 kHz, and 4.78 and 5.02 kHz, respectively).

the rising- (falling-) tone element is associated with the hole (hill) in the electron phase space. By performing numerical simulations, the rising-tone elements have been reproduced in several studies (H. Chen et al., 2022; Katoh & Omura, 2011; Ke et al., 2020; Lu et al., 2019, 2021; Tao et al., 2017), while the studies of falling-tone elements are limited (Fujiwara et al., 2023; Nogi et al., 2020; Nunn & Omura, 2012; Soto-Chavez et al., 2014; Wu et al., 2020). Soto-Chavez et al. (2014) and Fujiwara et al. (2023) proposed that falling tone elements can be formed in a homogeneous field. While Nunn and Omura (2012) and Wu et al. (2020) suggested that these elements are formed in the magnetic field with a negative inhomogeneity, which would require the waves propagating from high latitudes toward the equator. Nevertheless, Nogi et al. (2020) indicated this restriction is unnecessary, by producing falling-tone elements during poleward propagation.

In general, a chorus element can be composed of several “subpackets” (or “subelements,” with a duration of about 5–10 ms; R. Chen et al., 2022; Santolik et al., 2003; Tsurutani et al., 2020; Zhang et al., 2019), whose frequency either has the same chirping direction as the element, or is almost constant (R. Chen et al., 2022; Tsurutani et al., 2020). However, Liu et al. (2021) reported two unusual rising-tone elements. Although the central frequency of the constituent subpackets is upward chirping, the frequency of a single subpacket is surprisingly downward chirping. In Figure 1a, we replot the magnetic spectrum of the first chorus element in Liu et al. (2021). The wave frequency (calculated by the periods of zero-crossing of the magnetic field component along the maximum variance direction) is shown in Figure 1b, containing alternating upward chirping and downward chirping intervals. To investigate the spectrum in detail, we choose 4 instants (marked by the arrows in Figure 1b): $t = 53.86$ and 53.90 s during upward chirping intervals, and $t = 53.83$ and 53.88 s during downward

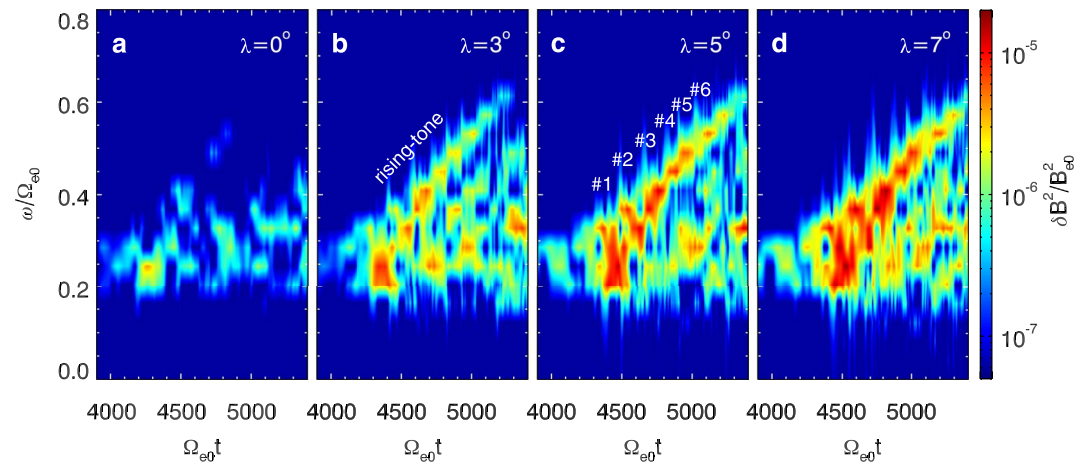


Figure 2. The $\omega - t$ spectrum of magnetic field at the latitudes of $\lambda =$ (a) 0° , (b) 3° , (c) 5° , and (d) 7° . In panel (c), the subpackets are denoted by different numbers.

chirping intervals. Figures 1c–1f show the corresponding spectra as a function of frequency, with two peaks (marked by dashed lines) in each spectrum. The generation of this kind of chirping is a mystery and is of interest in the present investigation. In this study, with the one-dimensional (1D) general curvilinear particle-in-cell (gcPIC) δf simulation model, we first reproduce the rising-tone elements with subpackets of downward chirping, and then investigate the associated electron structures in the phase space.

2. Simulation Model and Initial Setup

The general curvilinear plasma simulation code (gcPIC) software package contains three models: the gcPIC model (Ke et al., 2020; Lu et al., 2019), the gcPIC- δf model (H. Chen et al., 2022; Lu et al., 2021), and the gcPIC-hybrid model (Lu et al., 2022). To study the frequency chirping in chorus waves, we employ the 1-D gcPIC- δf simulation model in the dipole magnetic field. The δf method can reduce numerical noises significantly (Hu & Krommes, 1994; Sydora, 2003), where the velocity distribution f can be divided into $f = f_0 + \delta f$ (f_0 is the initial velocity distribution) and only the disturbed distribution δf is updated. The simulation domain is along the background magnetic field line, and reflecting and absorbing boundary conditions are used for particles and waves, respectively. There are three kinds of particles in the system: protons, cold and energetic electrons. The ions are assumed to be immobile, since the gyrofrequency of ions is much lower than the frequency of chorus waves.

At the equator, the ratio between plasma frequency and electron gyrofrequency is set to be $\omega_{pe}/\Omega_{e0} = 5.0$ ($\omega_{pe} = \sqrt{n_{c0}e^2/m_e\epsilon_0}$, and $\Omega_{e0} = eB_{e0}/m_e$, where B_{e0} is the background magnetic field at the equator, and n_{c0} is the number density of cold electrons), which is a typical value at $L = 6$. The energetic electrons are assumed to satisfy a bi-Maxwellian distribution, and the number density, parallel plasma beta, and temperature anisotropy of energetic electrons at the equator are $n_{heq}/n_{c0} = 0.005$, $\beta_{\parallel heq} = n_{heq}T_{\parallel 0}/(B_{e0}^2/2\mu_0) = 0.0048$ and $T_{\perp eq}/T_{\parallel eq} = 6$, respectively. Then, the electron distributions along the field line can be obtained by using the Liouville's theorem (Summers et al., 2012). To save computing resources, the topology of the background magnetic field equals that at $L = 0.5$. In the simulation domain, there are 5,000 grid cells (with a cell length of $0.19V_{Ae0}/\Omega_{e0}$, $V_{Ae0} = B_{e0}/\sqrt{\mu_0 n_{c0} m_e}$ is the electron Alfvén speed at the equator) over the latitudinal range from -31.5° to 31.5° , and 4,000 particles in each cell on average. The time step is set as $\Delta t = 0.03\Omega_{e0}^{-1}$.

3. Simulation Results

With a sliding window of 256 points and a time step of 2 points, we perform a fast Fourier transformation to the fluctuation magnetic field δB ($\delta B = \sqrt{\delta B_{\perp 1}^2 + \delta B_{\perp 2}^2}$, where $\delta B_{\perp 1}$ and $\delta B_{\perp 2}$ are two perpendicular components). Figure 2 shows the time-frequency spectra at the latitudes of $\lambda =$ (a) 0° , (b) 3° , (c) 5° , and (d) 7° . The waves are excited by temperature anisotropy of energetic electrons near the equator (Figure 2a), where the amplitudes are

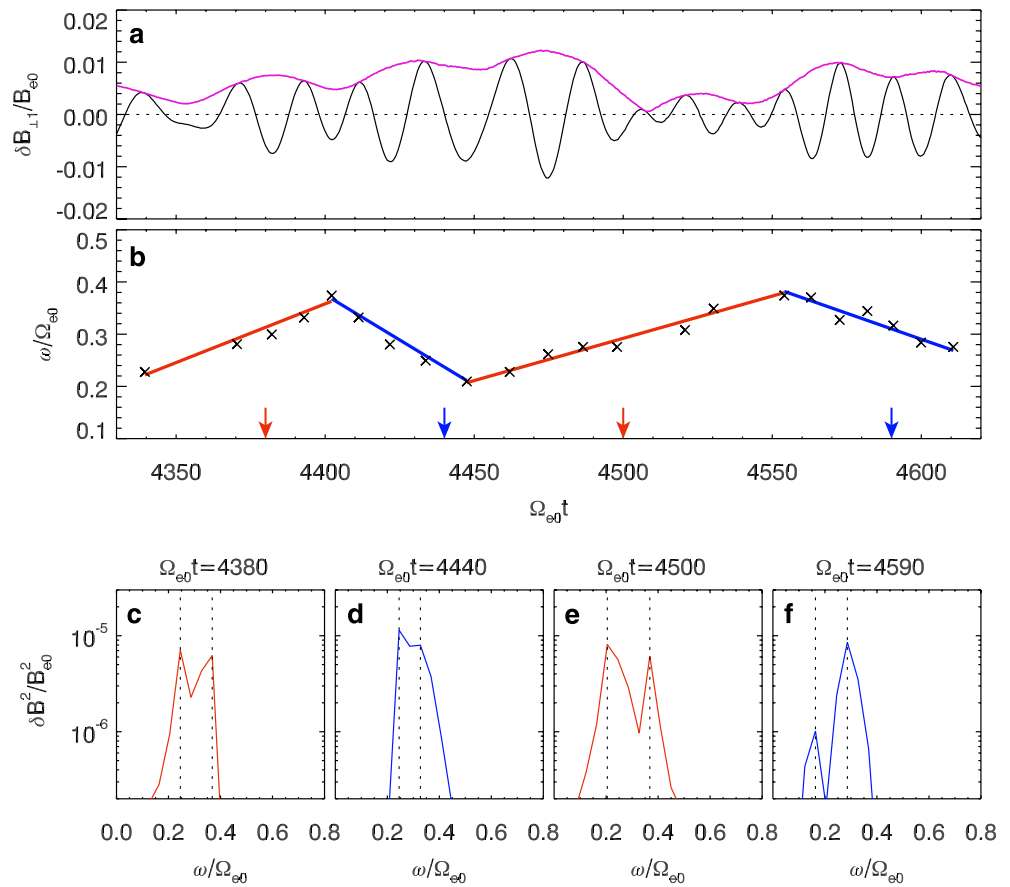


Figure 3. The temporal evolution of (a) magnetic field $\delta B_{\perp 1}$ (black line) and wave amplitude δB (magenta line), and (b) frequency ω (black crosses) at $\lambda = 5^\circ$. In panel (a), the dashed line denotes zero $\delta B_{\perp 1}$. In panel (b), the arrows denote the four selected instants ($\Omega_{e0}t = 4,380, 4,440, 4,500$, and $4,590$), and the red (blue) lines represent the linear fitting results in the upward (downward) chirping intervals. The spectra as a function of frequency at these four instants are shown in panels (c–f), where the red (blue) colors represent the intervals of upward (downward) chirping and the black dashed lines denote the two peaks of the spectrum.

weak and the spectrum doesn't have a clear discrete structure. Then, the waves propagate poleward, and their intensity gradually increases. At $\lambda = 3^\circ$ (Figure 2b), a rising-tone element occurs at $\Omega_{e0}t \approx 4,270$ with $\omega/\Omega_{e0} \approx 0.18$ and stops at $\Omega_{e0}t \approx 5,200$ with $\omega/\Omega_{e0} \approx 0.62$. It contains several subpackets, which are more visible at higher latitudes (Figures 2c–2d). At $\lambda = 5^\circ$, there exist 6 subpackets in total, whose intensity decreases as their frequencies increase. These subpackets are closely packed and are partially time-overlapped. Interestingly, the first and the second subpackets ($\Omega_{e0}t = 4,340$ – $4,620$) exhibit downward frequency chirping (with ω/Ω_{e0} changing from 0.35 to 0.2 and from 0.38 to 0.27, respectively), and still exist when the waves saturate at $\lambda \approx 15^\circ$. The downward chirping subpackets inside the rising-tone element resemble those in Figure 1a.

The details of the frequency chirping at $\lambda = 5^\circ$ in the interval of the first two subpackets are shown in Figure 3, including the temporal evolution of the (a) $\delta B_{\perp 1}$ component (black line) and amplitude δB (magenta line), and (b) frequency ω (black crosses). The ω for each half circle is estimated by the time interval between the start time and stop time of the zero crossing of the $\delta B_{\perp 1}$ component (Tsurutani et al., 2020), and such an estimate is only made for the half circles with peak amplitude $\delta B/B_{e0}$ greater than 0.003. As shown in Figure 3b, the waveform contains alternative intervals of upward chirping ($\Omega_{e0}t = 4,340$ – $4,401$ and $4,447$ – $4,553$) and downward chirping ($\Omega_{e0}t = 4,401$ – $4,447$ and $4,553$ – $4,620$), which is consistent with the observation in Figure 1b. Moreover, the amplitudes in the upward intervals (with a mean value of $\delta B/B_{e0} = 0.0057$) are comparable with those in the downward intervals (with a mean value of $\delta B/B_{e0} = 0.0079$).

To estimate the chirping rate $\Gamma = \partial\omega/\partial t$ from the waveform, we perform a linear fitting to the temporal evolution of ω , and the fitting results in the two intervals of upward (downward) chirping are represented by red (blue)

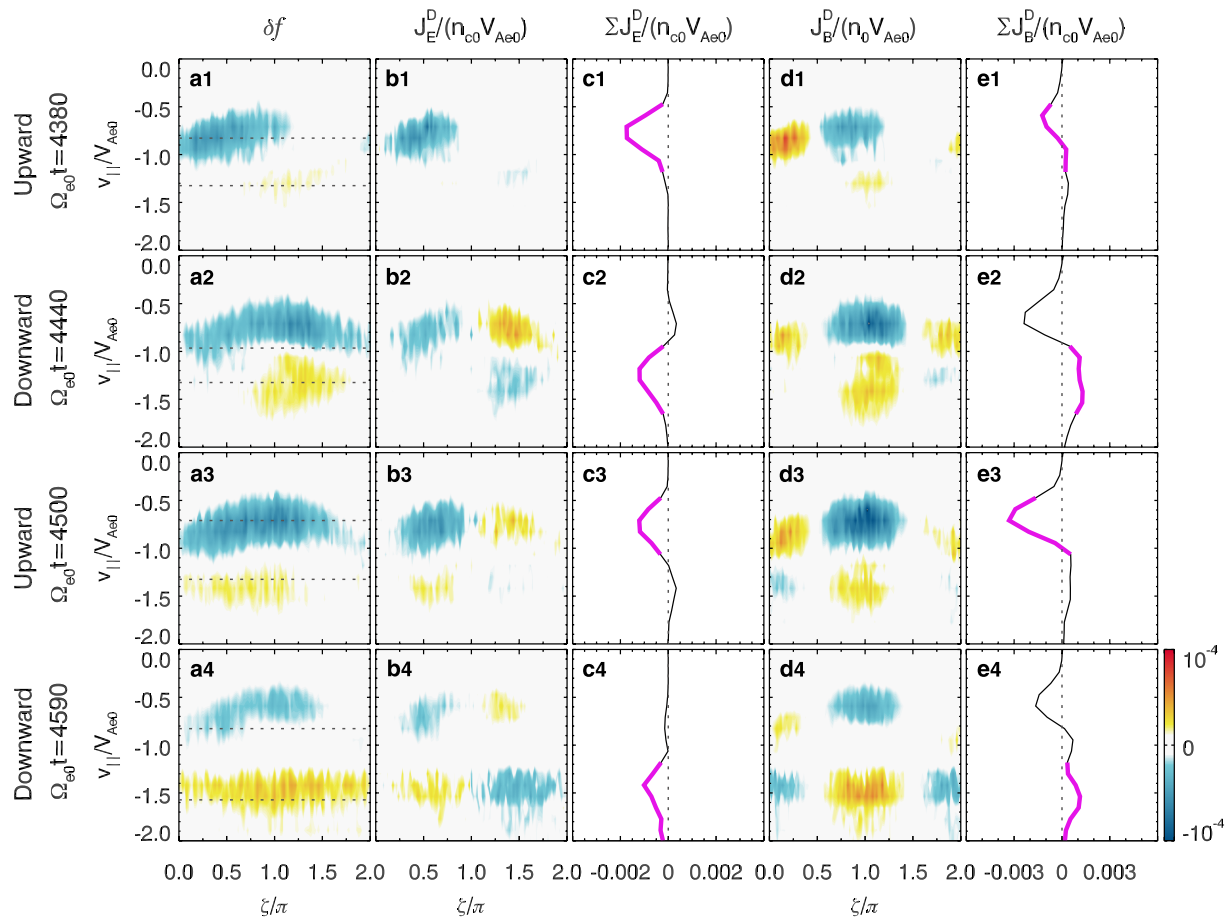


Figure 4. (a1–a4) The disturbed electron distribution δf , (b1–b4) resonant currents J_E^D , and (d1–d4) J_B^D in the ζ - v_{\parallel} plane at $\lambda = 5^\circ$ and $v_{\perp}/V_{Ae0} = 1.97$ – 2.95 . The panels from the top to the bottom denote different instants. The dashed lines in panels (a1–a4) represent theoretical resonant velocities v_r . The net integrated (c1–c4) $\sum J_E^D$ and (e1–e4) $\sum J_B^D$ as a function of v_{\parallel} . The dashed lines represent zero $\sum J_E^D$ or $\sum J_B^D$, and the thick magenta lines highlight the $\sum J_E^D$ and $\sum J_B^D$ corresponding to $\sum J_E^D < -0.0002$.

lines in Figure 3b. The Γ is defined as the slope of the fitting line, which equals $2.3 \times 10^{-3} \Omega_{e0}^2$, $-3.2 \times 10^{-3} \Omega_{e0}^2$, $1.5 \times 10^{-3} \Omega_{e0}^2$, and $-2.2 \times 10^{-3} \Omega_{e0}^2$ in each interval. We further compare these chirping rates with the theoretical values given by Omura et al. (2008):

$$S = -\frac{1}{\omega_r^2 \chi^2} \left\{ \gamma \left(1 - \frac{v_r}{v_g} \right)^2 \frac{\partial \omega}{\partial t} + \left[\frac{k \gamma v_{\perp}^2}{2 \Omega_e} - \left(1 + \frac{\chi^2}{2} \frac{\Omega_e - \gamma \omega}{\Omega_e - \omega} \right) v_r \right] \frac{\partial \Omega_e}{\partial h} \right\} \quad (1)$$

where S is the inhomogeneity term, $\omega_r^2 = k v_{\perp} e \delta B / m_e$ is the trapping frequency with the electron perpendicular velocity v_{\perp} , $\chi^2 = 1 - \omega^2 / (c^2 k^2)$ with the light speed c , γ is the relativistic factor, $v_r = (\omega - \Omega_e / \gamma) / k$ is the resonant velocity, $v_g = \partial \omega / \partial k$ is the group velocity, and h is the distance away from the equator. Here, S is set to be -0.4 (0.4) to maximize the energy transfer between electrons and waves during upward (downward) chirping intervals (Omura et al., 2008). The δB is chosen as the largest wave amplitude in each interval ($\delta B / B_{e0} = 0.0074$, 0.0102 , 0.0121 , and 0.0098 , respectively), and ω is the corresponding frequency ($\omega / \Omega_{e0} = 0.3208$, 0.2651 , 0.2392 , and 0.3512 , respectively). Then the wave number k is estimated by the cold plasma dispersion relation. The v_{\perp} is set to be $2.5 V_{Ae0}$, since the trapping electrons are mainly around this value (Figure 4). The theoretical chirping rates in the four intervals are $9.6 \times 10^{-4} \Omega_{e0}^2$, $-1.5 \times 10^{-3} \Omega_{e0}^2$, $9.2 \times 10^{-4} \Omega_{e0}^2$, and $-1.1 \times 10^{-3} \Omega_{e0}^2$, respectively, which are comparable with the values in simulation.

We then choose 4 instants (marked by the arrows in Figure 3b): $\Omega_{e0} t = 4,380$ and $4,500$ during upward chirping intervals, and $\Omega_{e0} t = 4,440$ and $4,590$ during downward chirping intervals. Figure 3c–3f show the spectrum of

δB^2 as a function of ω at each of the four instants. Interestingly, each spectrum has two peaks, which is also consistent with the observations (Figures 1c–1f). The frequencies of the peaks ω_p are denoted by dashed lines, with $\omega_p/\Omega_{e0} = 0.245$ and 0.368 , 0.245 and 0.327 , 0.205 and 0.368 , 0.205 and 0.327 , respectively. These frequencies are used for the calculation of theoretical resonant velocities in Figure 4.

The electron phase space densities during these four instants at $\lambda = 5^\circ$ are further investigated to understand the formation of upward and downward chirping. Figure 4 shows the (a1–a4) electron velocity distribution δf (b1–b4) differential resonant currents J_E^D and (d1–d4) differential resonant current J_B^D in the ζ - v_{\parallel} plane (where ζ is the angle between v_{\perp} and δB) at the four instants. The J_E^D and J_B^D are defined as

$$J_E^D(u_{\parallel}, \zeta) = \int_{u_{\perp 1}}^{u_{\perp 2}} \left[-e\bar{v}_{\perp} \cdot \widehat{\delta E} \right] \delta f(u_{\parallel}, \zeta, u_{\perp}) u_{\perp} du_{\perp} \quad (2)$$

$$J_B^D(u_{\parallel}, \zeta) = \int_{u_{\perp 1}}^{u_{\perp 2}} \left[-e\bar{v}_{\perp} \cdot \widehat{\delta B} \right] \delta f(u_{\parallel}, \zeta, u_{\perp}) u_{\perp} du_{\perp} \quad (3)$$

where $\widehat{\delta E}$ and $\widehat{\delta B}$ are the unit vectors of the disturbed electric field and magnetic field, $\delta f(u_{\parallel}, \zeta, u_{\perp})$ is the disturbed phase space density, $u_{\parallel} = \gamma v_{\parallel}$ and $u_{\perp} = \gamma v_{\perp}$ are the parallel and perpendicular momentums, and $u_{\perp 1}$ and $u_{\perp 2}$ are the lower and upper limits of u_{\perp} . The J_E^D and J_B^D are the differential forms of resonant current J_E and J_B (Omura, 2021), where the positive (negative) J_E^D means the energy is transferred from waves (electrons) to electrons (waves), and the positive (negative) J_B^D means the frequency is downward (upward) chirping (Omura et al., 2008). In this study, J_E^D and J_B^D are calculated by using the hot electrons with $v_{\perp}/V_{Ae0} = 1.97$ – 2.95 , since the electrons with a pitch angle of $\sim 60^\circ$ are more easily affected by the nonlinear interactions with chorus waves (Zhang et al., 2019). The dashed lines in Figures 4a1–4a4 represent theoretical resonant velocities v_r by using the frequencies of the two peaks ω_p in each spectrum (Figures 3c–3f), where the small $|v_r|$ corresponds to the larger ω_p . We also integrate $J_E^D(\zeta, v_{\parallel})$ and $J_B^D(\zeta, v_{\parallel})$ over ζ , and plot the $\sum J_E^D$ and $\sum J_B^D$ as a function of v_{\parallel} in Figures 4c1–4c4 and 4e1–4e4, where the dashed lines denote zero $\sum J_E^D$ or $\sum J_B^D$. Then we use thick magenta lines to highlight the resonant currents ($\sum J_E^D$ and $\sum J_B^D$) contributing to the wave growth (with a negative $\sum J_E^D < -0.0002$).

At each time instant, both a hole and a hill are formed around v_r in the phase space, where the hole (hill) represents the structure with a number density much lower (higher) than the surrounding and the resonant electrons are restricted in a finite range of ζ (the hole and hill structures are also detected in the full distribution f , as shown in Supporting Information S1). At the first instant $\Omega_{e0}t = 4,380$ with the upward chirping (Figures 4a1–4e1), a hole exists at $\zeta \approx 0 - \pi$ around $v_r/V_{Ae0} = -0.828$, which causes a negative J_E^D at $\zeta \sim \pi/2$. Moreover, it can contribute to a positive J_B^D at $\zeta \approx 0$ and a negative J_B^D at $\zeta \approx \pi$, with a net integrated $\sum J_B^D < 0$. Therefore, the waves with an upward chirping can be excited. Besides, there is also a hill at $\zeta \approx \pi - 3\pi/2$ around $v_r/V_{Ae0} = -1.325$, but it is so weak that the corresponding $\sum J_E^D$ and $\sum J_B^D$ are both close to 0. At the third instant $\Omega_{e0}t = 4,500$ (Figures 4a3–4e3), there exists a hole at $\zeta \approx 0 - 3\pi/2$ around $v_r/V_{Ae0} = -0.710$, and a hill at $\zeta \approx 0 - \pi$ around $v_r/V_{Ae0} = -1.325$. The hole contributes to a negative $\sum J_B^D$, while the hill corresponds to a positive $\sum J_B^D$. However, since the hole provides a negative $\sum J_E^D$, only the upward chirping waves can gain energy.

At the other two instants, $\Omega_{e0}t = 4,440$ and $\Omega_{e0}t = 4,590$, there also exist holes in the phase space, but they cannot provide free energies for wave excitation, since the corresponding $\sum J_E^D$ is close to or even larger than 0. While the electron hills, which mainly occur in the range of $\zeta \approx \pi - 2\pi$, are responsible for the downward chirping since they contribute to a positive J_B^D at $\zeta \approx \pi$ and a negative J_B^D at $\zeta \approx 3\pi/2$. This suggests that although both hole and hill structures are formed during either upward chirping or downward chirping intervals, only one of the two contributes to $J_E^D < 0$ and causes wave excitation. The chirping direction is determined by the corresponding J_B^D . In other words, the upward chirping is related to the hole at $\zeta \approx 0 - \pi$, while the hill at $\zeta \approx \pi - 2\pi$ is associated with the downward chirping.

4. Conclusions and Discussion

By performing a 1D gcPIC- δf simulation in the dipole field, we reproduce the rising-tone chorus element with subpackets of a downward chirping, resembling the observations in Liu et al. (2021). The frequency contains both upward and downward chirping intervals, and their chirping rates are roughly consistent with the theoretical values. During an interval of upward or downward chirping, both hole and hill structures can be formed around the theoretical resonant velocities. However, only one structure (either a hole or a hill) can contribute to the chirping. The upward chirping is associated with the hole at $\zeta \approx 0 - \pi$, which can cause a negative J_E^D at $\zeta \sim \pi/2$ and a negative J_B^D at $\zeta \sim \pi$. While the downward chirping is related to the hill at $\zeta \approx \pi - 2\pi$, with a negative J_E^D at $\zeta \sim 3\pi/2$ and a positive J_B^D at $\zeta \sim \pi$. Our study identifies a novel structure of electron hill-hole combination in the phase space that is responsible for the frequency chirping alternation in chorus waves.

The generation mechanism of frequency chirping has become a hot topic recently. Previous theoretical analysis has indicated that there is only a single electron structure (either a hole or a hill) when the frequency chirps (Omura et al., 2008; Tao et al., 2017). This is further supported by numerical simulations, where there is a hole accompanied by upward chirping (H. Chen et al., 2022; Katoh & Omura, 2011; Tao et al., 2017), and a hill associated with downward chirping (Nogi et al., 2020; Nunn & Omura, 2012). However, both hole and hill can be formed in our study, no matter whether the frequency is upward or downward chirping. The hole and hill compete by contributing to different signs of differential resonant currents J_E^D and J_B^D , and the dominant one can determine the wave growth and chirping direction. The hole-hill combination could be a general scenario in the electron phase space during frequency chirping, which may invoke a new theoretical model to investigate the frequency chirping. Nevertheless, previous studies may only detect the dominant structure, since another one might be weak and cannot exist for a long time. As shown in Figures 1a and 2, the subpackets are not entirely separated, but packed closely in the spectrum. Therefore, there are two frequency peaks in the spectrum, which are detected in both satellite observation (Figures 1c–1f) and in simulation (Figures 3c–3f). Moreover, the positions of holes and hills are consistent with the resonant velocities given by the frequencies of the peaks, further supporting the existence of both upward chirping and downward chirping. However, the generation of the two peaks is still a mystery, which is beyond the scope of this study and left to future work. Our study provides a comprehensive understanding of how the electron structure in the phase space affects the frequency chirping of chorus waves.

Data Availability Statement

The data from Van Allen Probes were from <https://spdf.gsfc.nasa.gov/pub/data/rbsp/>. The simulation data can be accessed at <https://doi.org/10.5281/zenodo.7452974>.

References

- Burtis, W. J., & Helliwell, R. A. (1969). Banded chorus a new type of VLF radiation observed in the magnetosphere by OGO 1 and OGO 3. *Journal of Geophysical Research*, 74(11), 3002–3010. <https://doi.org/10.1029/JA074i011p03002>
- Chen, H., Lu, Q., Wang, X., Fan, K., Chen, R., & Gao, X. (2022). One-dimensional gcPIC- δf simulation of hooked chorus waves in the Earth's inner magnetosphere. *Geophysical Research Letters*, 49(4), e2022GL097989. <https://doi.org/10.1029/2022GL097989>
- Chen, R., Tsurutani, B. T., Gao, X., Lu, Q., Chen, H., Lakhina, G. S., & Hajra, R. (2022). The structure and microstructure of rising-tone chorus with frequencies crossing at $f \sim 0.5 f_{ce}$. *Journal of Geophysical Research: Space Physics*, 127(8), e2022JA030438. <https://doi.org/10.1029/2022JA030438>
- Fujiwara, Y., Omura, Y., & Nogi, T. (2023). Triggering of whistler-mode rising and falling tone emissions in a homogeneous magnetic field. *Journal of Geophysical Research: Space Physics*, 128(2), e2022JA030967. <https://doi.org/10.1029/2022JA030967>
- Gao, X., Chen, R., Lu, Q., Chen, L., Chen, H., & Wang, X. (2022). Observational evidence for the origin of repetitive chorus emissions. *Geophysical Research Letters*, 49(12), e2022GL099000. <https://doi.org/10.1029/2022GL099000>
- Helliwell, R. A. (1967). A theory of discrete VLF emissions from the magnetosphere. *Journal of Geophysical Research*, 72(19), 4773–4790. <https://doi.org/10.1029/jz072i019p04773>
- Horne, R. B., & Thorne, R. M. (1998). Potential waves for relativistic electron scattering and stochastic acceleration during magnetic storms. *Geophysical Research Letters*, 25(15), 3011–3014. <https://doi.org/10.1029/98GL01002>
- Hu, G., & Krommes, J. A. (1994). Generalized weighting scheme for δf particle-simulation method. *Physics of Plasmas*, 1(4), 863–874. <https://doi.org/10.1063/1.870745>
- Katoh, Y., & Omura, Y. (2011). Amplitude dependence of frequency sweep rates of whistler mode chorus emissions. *Journal of Geophysical Research*, 116(A7), A07201. <https://doi.org/10.1029/2011JA016496>
- Ke, Y., Lu, Q., Gao, X., Wang, X., Chen, L., Wang, S., & Wang, S. (2020). Particle-in-cell simulations of characteristics of rising-tone chorus waves in the inner magnetosphere. *Journal of Geophysical Research: Space Physics*, 125(7), e2020JA027961. <https://doi.org/10.1029/2020JA027961>

Acknowledgments

This work was supported by the Grants NASA-80NSSC21K1688 and NASA-80NSSC21K1679.

- Li, W., Bortnik, J., Thorne, R. M., Cully, C. M., Chen, L., Angelopoulos, V., et al. (2013). Characteristics of the Poynting flux and wave normal vectors of whistler-mode waves observed on THEMIS. *Journal of Geophysical Research: Space Physics*, *118*(4), 1461–1471. <https://doi.org/10.1002/jgra.50176>
- Liu, S., Gao, Z., Xiao, F., He, Q., Li, T., Shang, X., et al. (2021). Observation of unusual chorus elements by van Allen Probes. *Journal of Geophysical Research: Space Physics*, *126*(7), e2021JA029258. <https://doi.org/10.1029/2021JA029258>
- Lu, Q., Chen, L., Wang, X., Gao, X., Lin, Y., & Wang, S. (2021). Repetitive emissions of rising-tone chorus waves in the inner magnetosphere. *Geophysical Research Letters*, *48*(15), e2021GL094979. <https://doi.org/10.1029/2021GL094979>
- Lu, Q., Guo, J., Lu, S., Wang, X., Slavin, J. A., Sun, W., et al. (2022). Three-dimensional Global hybrid simulations of flux transfer event showers at Mercury. *The Astrophysical Journal*, *937*, 1. <https://doi.org/10.3847/1538-4357/ac8bcf>
- Lu, Q., Ke, Y., Wang, X., Liu, K., Gao, X., Chen, L., & Wang, S. (2019). Two-dimensional general curvilinear particle-in-cell (gcPIC) simulation of rising-tone chorus waves in a dipole magnetic field. *Journal of Geophysical Research: Space Physics*, *124*(6), 4157–4167. <https://doi.org/10.1029/2019ja026586>
- Nishimura, Y., Bortnik, J., Li, W., Thorne, R. M., Ni, B., Lyons, L. R., et al. (2013). Structures of dayside whistler-mode waves deduced from conjugate diffuse aurora. *Journal of Geophysical Research: Space Physics*, *118*(2), 664–673. <https://doi.org/10.1029/2012ja018242>
- Nogi, T., Nakamura, S., & Omura, Y. (2020). Full particle simulation of whistler-mode triggered falling-tone emissions in the magnetosphere. *Journal of Geophysical Research: Space Physics*, *125*(10), e2020JA027953. <https://doi.org/10.1029/2020JA027953>
- Nunn, D., & Omura, Y. (2012). A computational and theoretical analysis of falling frequency VLF emissions. *Journal of Geophysical Research*, *117*(A8), A08228. <https://doi.org/10.1029/2012JA017557>
- Omura, Y. (2021). Nonlinear wave growth theory of whistler-mode chorus and hiss emissions in the magnetosphere. *Earth Planets and Space*, *73*(1), 95. <https://doi.org/10.1186/s40623-021-01380-w>
- Omura, Y., Katoh, Y., & Summers, D. (2008). Theory and simulation of the generation of whistler-mode chorus. *Journal of Geophysical Research*, *113*(A4), A04223. <https://doi.org/10.1029/2007JA012622>
- Santolik, O., Gurnett, D. A., Pickett, J. S., Parrot, M., & Cornilleau-Wehrlin, N. (2005). Central position of the source region of storm-time chorus. *Planetary and Space Science*, *53*(1–3), 299–305. <https://doi.org/10.1016/j.pss.2004.09.056>
- Santolik, O., Gurnett, D. A., Pickett, J. S., Parrot, M., & Cornilleau-Wehrlin, N. (2003). Spatio-temporal structure of storm-time chorus. *Journal of Geophysical Research*, *108*(A7), 1278. <https://doi.org/10.1029/2002JA009791>
- Soto-Chavez, A. R., Wang, G., Bhattacharjee, A., Fu, G. Y., & Smith, H. M. (2014). A model for falling-tone chorus. *Geophysical Research Letters*, *41*(6), 1838–1845. <https://doi.org/10.1002/2014GL059320>
- Summers, D., Omura, Y., Miyashita, Y., & Lee, D. H. (2012). Nonlinear spatiotemporal evolution of whistler mode chorus waves in Earth's inner magnetosphere. *Journal of Geophysical Research*, *117*(A9), A09206. <https://doi.org/10.1029/2012ja017842>
- Summers, D., Thorne, R. M., & Xiao, F. L. (1998). Relativistic theory of wave-particle resonant diffusion with application to electron acceleration in the magnetosphere. *Journal of Geophysical Research*, *103*(A9), 20487–20500. <https://doi.org/10.1029/98JA01740>
- Sydora, R. D. (2003). *Low noise electrostatic and electromagnetic δf particle-in-cell simulation of plasmas, Space Plasma Simulation*. In J. Buchner, C. T. Dum, & M. Scholer (Eds.), (pp. 109–124). LNP 615.
- Tao, X., Zonca, F., & Chen, L. (2017). Identify the nonlinear wave-particle interaction regime in rising tone chorus generation. *Geophysical Research Letters*, *44*(8), 3441–3446. <https://doi.org/10.1002/2017GL072624>
- Thorne, R. M., Li, W., Ni, B., Ma, Q., Bortnik, J., Chen, L., et al. (2013). Rapid local acceleration of relativistic radiation-belt electrons by magnetospheric chorus. *Nature*, *504*(7480), 411–414. <https://doi.org/10.1038/nature12889>
- Thorne, R. M., Ni, B., Tao, X., Horne, R. B., & Meredith, N. P. (2010). Scattering by chorus waves as the dominant cause of diffuse auroral precipitation. *Nature*, *467*(7318), 943–946. <https://doi.org/10.1038/nature09467>
- Tsurutani, B. T., Chen, R., Gao, X., Lu, Q., Pickett, J. S., Lakhina, G. S., et al. (2020). Lower-band “monochromatic” chorus riser subelement/wave packet observations. *Journal of Geophysical Research: Space Physics*, *125*(10), e2020JA028090. <https://doi.org/10.1029/2020JA028090>
- Tsurutani, B. T., & Smith, E. J. (1974). Postmidnight chorus: A substorm phenomenon. *Journal of Geophysical Research*, *79*(1), 118–127. <https://doi.org/10.1029/JA079i001p00118>
- Turner, D. L., Lee, J. H., Claudepierre, S. G., Fennell, J. F., Blake, J. B., Jaynes, A. N., et al. (2017). Examining coherency scales, substructure, and propagation of whistler mode chorus elements with Magnetospheric Multiscale (MMS). *Journal of Geophysical Research: Space Physics*, *122*(11), 11201–11226. <https://doi.org/10.1002/2017JA024474>
- Wu, Y., Tao, X., Zonca, F., Chen, L., & Wang, S. (2020). Controlling the chirping of chorus waves via magnetic field inhomogeneity. *Geophysical Research Letters*, *47*, e2020GL087791. <https://doi.org/10.1029/2020GL087791>
- Xiao, F., Yang, C., He, Z., Su, Z., Zhou, Q., He, Y., et al. (2014). Chorus acceleration of radiation belt relativistic electrons during March 2013 geomagnetic storm. *Journal of Geophysical Research: Space Physics*, *119*(5), 3325–3332. <https://doi.org/10.1002/2014JA019822>
- Zhang, X.-J., Mourenas, D., Artemyev, A. V., Angelopoulos, V., Bortnik, J., Thorne, R. M., et al. (2019). Nonlinear electron interaction with intense chorus waves: Statistics of occurrence rates. *Geophysical Research Letters*, *46*(13), 7182–7190. <https://doi.org/10.1029/2019GL083833>